MATERIALS CHEMISTRY FRONTIERS

# Colloidal Au-Cu Alloy Nanoparticles: Synthesis, Optical Properties and Applications



| | |
|---|---|
| Journal: | *Materials Chemistry Frontiers* |
| Manuscript ID | QM-REV-11-2017-000538.R2 |
| Article Type: | Review Article |
| Date Submitted by the Author: | 30-Mar-2018 |
| Complete List of Authors: | Thota, Sravan; University of Connecticut, Chemistry<br>Wang, Yongchen; University of Connecticut, Chemistry<br>Zhao, Jing; University of Connecticut, Chemistry |
| | |

# Colloidal Au-Cu Alloy Nanoparticles: Synthesis, Optical Properties and Applications

Sravan Thota[a], Yongchen Wang[a] and Jing Zhao[a,b*]

[a.] *Department of Chemistry, University of Connecticut, 55 North Eagleville Road, Storrs, Connecticut 06269-3060, United States.*

[b.] *Institute of Materials Science, University of Connecticut, Storrs, Connecticut 06269-3136, United States.*

## Contents

## Abstract

In this review, we discuss the recent advancement in the shape-controlled synthesis and characterization of colloidal Au-Cu alloy nanostructures. Then we review the studies on the plasmonic properties of the Au-Cu alloy nanoparticles, which are different from that of the nanoparticles composed of pure Au or Cu due to the synergism between Au and Cu. The Au-Cu nanoparticles with tunable composition and geometry have been applied in heterogeneous catalysis for $CO_2$ reduction reaction and many other reactions and have shown good catalytic activity. They have also been demonstrated to be effective in killing tumor cells using photothermal therapy. At the end of this review, we provide our perspective on the future work of the synthesis and applications of Au-Cu alloy nanoparticles.

## 1. Introduction

Metals exhibit unique catalytic, magnetic and optical properties when they are reduced to nanometer dimensions.[1-8] The physical properties of metals at the nanoscale are different from that of the bulk and single atomic state. Phase miscibility is one such property where metals that are not mixable at the bulk scale can form alloy at the nanometer regime, which provides opportunity to combine different elements forming bi- or multi- metallic alloy nanoparticles.[9-12] These nanoparticles exhibit enhanced functionalities compared to their parent component due to the effect caused by mixing the elements. Therefore, the metal alloy systems are of great interest for plasmonic (such as Au-Ag) and electrochemical catalytic (such as Pt-Pd) applications. Many bimetallic systems of different morphologies and configurations have been fabricated, composed of Au-Ag, Au-Pd, Au-Pt, Ag-Cu, Pd-Pt, Pd-Rh, Pt-Ag, and so on.[13-26] Recently, Au-Cu alloy system emerged as another promising alloy system, which has shown excellent applications in catalysis, photonics and biomedical research.[27-29]

Au and Cu nanoparticles are both excellent plasmonic and catalytic materials. For example, Au nanoparticles exhibit size and shape tunable optical properties, which are sensitive to their dielectric environment. Moreover, Au nanoparticles are stable, biocompatible, and their surfaces are easy to functionalize for chemical/bio conjugation. These properties allow them to be applied in bio sensing and imaging, photo thermal therapy, drug delivery, catalysis and pollution control.[30-36] Not only Au nanoparticles, Cu nanoparticles also show strong absorption in visible and near infrared (NIR) region with possible applications in photonics, sensing and imaging. Apart from plasmonic properties, Cu nanoparticles are promising heterogeneous catalysts for many chemical reactions such as oxidation of benzyl alcohol, propene and CO, and reduction of $CO_2$.[37-45] However, the applications of Cu nanoparticles was greatly restricted by their

susceptibility to oxidation, upon exposure to air. Oxidation of Cu to CuO or $Cu_2O$ eradicates their plasmonic properties and reduces their catalytic activity.[46, 47] Strategies like coating Cu nanoparticles with bulk ligands only helped in reducing the surface energy of nanoparticles, but could not prevent oxidation.[48, 49] One solution to improve the stability of Cu nanoparticles is to alloy Cu with stable metals such as Au, a strategy that has been already implemented at the bulk scale for many other metal alloys.[50, 51] When combining the two, Au-Cu alloy nanoparticles offer not only good stability and optical tunability, but also high catalytic activity, owing to the synergistic effect between the two components. Hence, Au-Cu alloy nanoparticles have recently been utilized for $CO_2$ reduction, *p*-nitrophenol reduction, partial oxidation of methanol to produce hydrogen fuels and catalytic oxidation of benzyl alcohol, CO and propene.[52-56]

In this review, we firstly discuss the Au-Cu phase diagram followed by synthetic strategies to fabricate Au-Cu alloy nanoparticles of various well-controlled shapes and compositions. We focus on the key factors that control the shape of the Au-Cu alloy nanoparticles like reducing agents, ligands, and reaction kinetics. Then we review the localized surface plasmon resonance (LSPR) of the Au-Cu alloy nanoparticles, and how the geometry and composition affect LSPR. We also discuss the plasmon damping effect and LSPR peak splitting caused by atomic level structural defects in Au-Cu alloy nanosystems. Next, we review the applications of the colloidal Au-Cu alloy nanosystems in catalysis and biomedical fields. Catalytic performance for $CO_2$ reduction, *p*-nitrophenol reduction, methanol oxidation, and CO oxidation was discussed for colloidal AuCu nanoparticles without focus on support films. The AuCu alloy/support for catalysis was discussed previously in a review by Hutchings and co-workers.[27] Lastly, we conclude and comment on the future scope of shape controlled synthesis of Au-Cu alloy nanostructures and their applications in heterogeneous catalysis.

**2. Au-Cu Phase Diagram**Understanding the phase transition of Au-Cu alloy at the nanoscale is critical for the synthesis of Au-Cu nanoparticles, but it is difficult to obtain the phase diagram experimentally. Fortunately, powerful theoretical tools have been applied to predict the phase diagrams of Au-Cu nanoparticles of varying sizes and shapes in recent years. According to empirical Hume–Rothery rules, whether an alloy can be formed with two metals

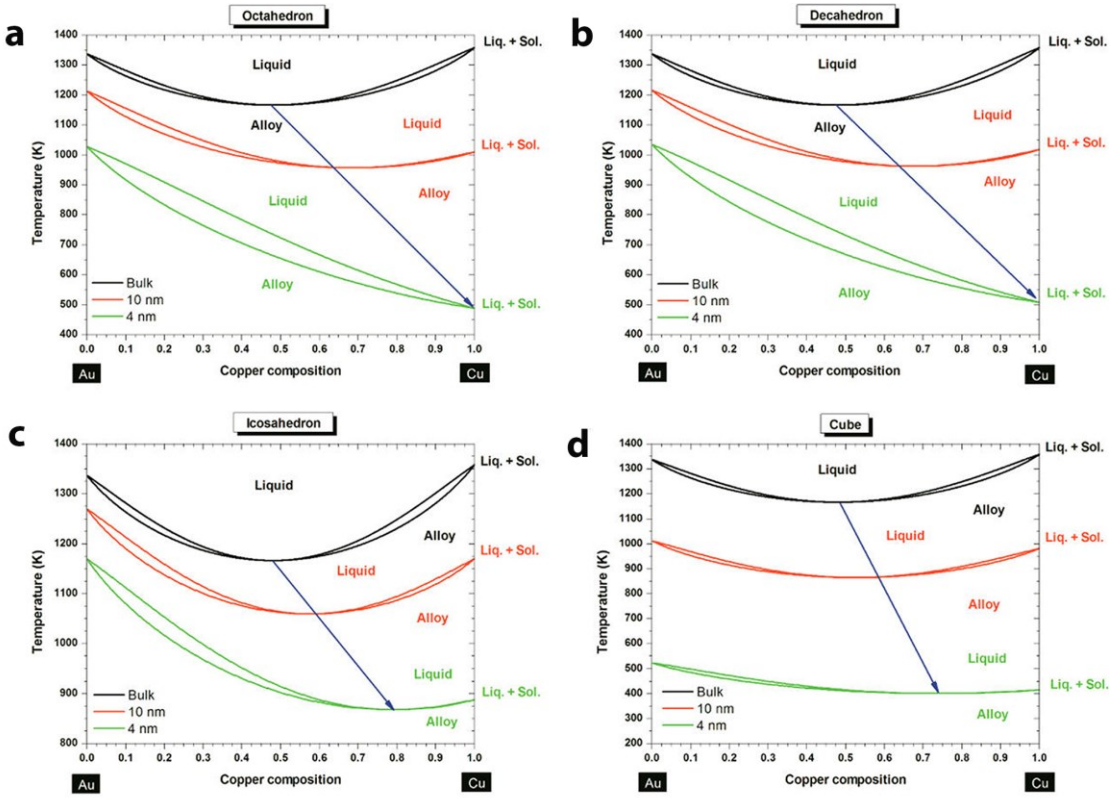


Figure 1. Phase diagrams of Au-Cu system at bulk scale (black), 10 nm (red) and 4 nm (green) for different shapes (a) octahedron, (b) decahedron, (c) icosahedron, (d) cube. The blue arrow indicates the size effect on the congruent melting point. Reproduced from Reference 60, with permission from American Chemical Society, Copyright 2013.

depend on the similarity of four factors: atomic radii, valence, crystal structure and electronegativity.[57, 58] Au and Cu satisfy three of these conditions as they share common crystal structure (*fcc*), valence (+1) and similar atomic radii (difference less than 15%). Hence, at the bulk scale Au and Cu form random substitutional solid solution at high temperature, and ordered solid solutions like $AuCu_3$, $Au_3Cu$ and AuCu at low temperatures. One interesting behavior of

Au-Cu alloy is congruency, which means the alloy's melting point is below its constituent elements and the alloy melts at a particular temperature (rather than over a range), just like a single metal. The phase diagram of Au-Cu at bulk indicates that the congruent melting point is at 910 °C with 44% Cu composition[59]. When the nanoscale phase diagram is considered for the Au-Cu alloy, size and shape factors have huge influence on the congruent melting point, as predicted by Jose-Yacaman and coworkers[60]. Specifically, Au-Cu nanoparticles with sizes of 10 nm and 4 nm are compared to the bulk for different shapes. As shown in Figure 1, above the liquidus curve, the solution is purely liquid, and below the solidus curve the solution is purely solid, and in between it is in solid-liquid equilibrium. From the simulated phase diagrams, a few conclusions can be drawn: i) liquidus and solidus curves move towards low temperature (which means a decrease in the stability of the nanoparticles) as size of alloy decreases from bulk to 4 nm; ii) congruent melting point decreases as size decreases; iii) the melting temperature, melting enthalpy and interaction parameters of the alloy nanoparticles are all size and shape dependent; iv) the most stable shapes of the Au-Cu nanoparticles are dodecahedron, truncated octahedron and icosahedron, regardless of the composition and the size of the nanoalloy. Later, Meng and co-workers[61] deduced similar conclusions. Another interesting finding is that surface segregation increases from bulk to nanoscale due to a higher surface-to-volume ratio.[59] Also, Au is preferred on the surface compared to Cu for all sizes and shapes of nanoparticles because Au atoms are larger than Cu atoms. When the larger atom of the alloy are on the surface, it would require fewer number of atoms to fill the surface (fewer broken bonds), reducing the overall surface energy. In addition, the crystal structures and facets also influence the surface segregation because there is a difference in the percentage of missing nearest neighboring atoms for the outmost layer[60] (i.e for atoms belonging to a (111) face in a face centered cubic structure, the

percentage of missing atoms would be 3/12=25%, while for atoms belonging to a (100) face in the same structure, the percentage would be 4/12=33%). This difference in the missing atoms will cause a difference in surface energy, which will affect metal composition on the surface. Overall, along with factors like size and shape, surface segregation would influence the congruent melting point and phases of Au-Cu alloys. Improving the understanding of phase diagram and surface segregation will be beneficial in terms of synthesizing specific Au-Cu alloy nanoparticles (i.e via thermal evolution[62]).

## 3. Synthesis of Au-Cu Alloy Nanostructures

Over the past decade, shape control of monometallic nanoparticles has been achieved using bottom up synthetic methods such as co-reduction, thermal decomposition, seed-mediated growth and galvanic replacement.[63-67] Based on the knowledge obtained from the synthesis of monometallic nanoparticles, many methods have been developed to fabricate bimetallic nanoparticles.[9, 68, 69] Similar to monometallic nanoparticles, morphology and crystal structures of the bimetallic nanoparticles are dictated by the reaction pathways, which can be controlled by the synthetic method and reaction conditions.[70-72] In this review, the synthetic protocols of Au-Cu alloy nanoparticles are broadly classified into co-reduction, seed mediated growth, combination of co-reduction and seed mediated growth, galvanic replacement and single source decomposition. When introducing each method, reaction kinetics and ligands are discussed in detail because they are important factors determining the configuration of the resulting Au-Cu nanostructures. Although the discussion is limited to the synthesis of Au-Cu alloy nanostructures in this review, the methods can be applied to other bimetallic nanosystems as well.

### *3.1 Co-reduction method*

Co-reduction is a one-step, straightforward synthetic method for generating Au-Cu alloy nanostructures. Generally, co-reduction requires two metal ions with similar reduction potentials or their reduction potentials need to be tuned by changing the molar ratios and/or the types of precursors, so that they can be reduced at a similar rate by a common reducing agent. The strength of the reducing agent determines the number of atoms available for nucleation at initial stages, which affects the shape of the resulting nanocrystals.[69, 71] Adjusting the metal precursors, surface ligands and the stoichiometric ratios of the reactants can change the reducing rates and also crystal growth direction, which allows for the fabrication Au-Cu alloy nanoparticles of various sizes, compositions and morphologies in a one-step co-reduction method.

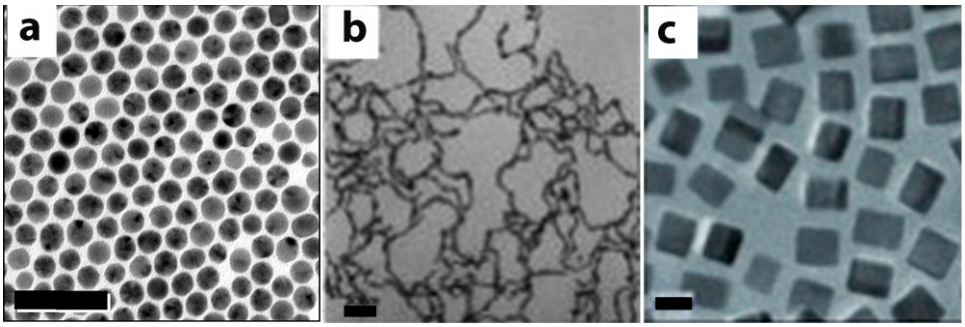


Figure 2. TEM images of Au-Cu alloy nanoparticles synthesized using co-reduction methods. (a) Spheres, scale bar=50 nm (b) nanowires, Scale bar=20 nm (c) nanocubes. Scale bar=5 nm. (a) Reproduced from reference 73, with permission from American Chemical Society, Copyright 2010. (b) Reproduced from reference 74, with permission from Wiley-VCH Verlag GmbH & Co. KGaA, Weinheim, Copyright 2012. (c)Reproduced from reference 75, with permission from Wiley-VCH Verlag GmbH & Co. KGaA, Weinheim, Copyright 2010.

For example, spherical Au-Cu alloy nanoparticles have been fabricated using a co-reduction method developed by Schaak and co-workers (Figure 2a). [73] In this method, 1-octadecene, oleic acid and oleylamine were used as the reducing agents and stabilizing ligands. By varying the amount of Cu precursor in the synthesis, $Au_{1-x}Cu_x$ alloy nanoparticles with *x* values varying from

0 to 0.5 were obtained. The nanospheres were around 8 nm in size, with uniform size distribution and disordered crystal structure as shown in Figure 2a. Not only spherical, but also Au-Cu alloy nanowires have been produced using a co-reduction method in the aqueous phase by Zhang and coworkers (Figure 2b).[74] $HAuCl_4$ and $Cu(NO_3)_2$ were used as the Au and Cu precusors respectively. $NaBH_4$ was used as a strong reducing agent in this protocol, created fast nucleation process at the initial stage of the reaction. A non-ionic surfactant Triton X-100 was used to weakly bind to the nucleation sites. It favored attachment of the Au and Cu atoms onto the specific nucleation sites, leading to the nanowire growth. The Au-Cu alloy nanowires were polycrystalline, with a diameter around 3.5 nm and a length of several hundred nanometers as shown in Figure 2b. Following these methods, co-reduction strategy was extended to fabricate complex three-dimensional geometries like nanocubes. Uniform single crystalline Au-Cu alloy nanocubes were synthesized by Liu and Walker[75] by co-reduction of $HAuCl_4$ and $Cu(acac)_2$ (Figure 2c). In this work 1,2-hexadecanediol was used as the reducing agent. 1,2-hexadecanediol, together with co-reducing agent 1-dodecanthiol controls the reduction rates of Cu(II) and Au(III) and also the nucleation process, which are critical for the formation of Au-Cu alloy nanocubes. In this work, cubes of edge lengths of 3.4, 5, 23, 45 and 85 nm with Au:Cu ratios between 3:1 to 1:3 were synthesized by varying the relative amount of precursors to reducing agent. Figure 2c displays nanocubes of edge length 5 nm with uniform size distribution. The studies discussed above show that the choice of the reducing agent and its interaction with Au and Cu precursor play a key role in shape and size control. In a word, co-reduction is the most straightforward and versatile method in bimetallic nanoparticles synthesis, but some complicated structures cannot be directly synthesized using the co-reduction method.

### *3.2 Seed-Mediated Growth*

Although co-reduction can generate Au-Cu alloy structures of a variety of morphologies, it is still challenging to find common conditions to control the reduction of both Au and Cu precursors simultaneously. The differences in the physicochemical properties of the precursors such as redox potential, crystal structure, and melting point cause inherent difficulties during the synthesis. Fine-tuning the morphology and composition at the same time is hard to achieve using the co-reduction method. In order to overcome these problems, seed mediated growth has been developed and has become the most popular method to generate Au-Cu nanostructures with complex morphologies.[71] In this strategy, a well-defined crystal made of Au is synthesized first and employed as the seed. The Au seeds then serve as hetero nucleation sites for the incoming Cu atoms to attach on. This sequential order provides a possibility to fabricate nanoparticles of special morphologies, such as nanorods.

Using the seed mediated strategy, a number of protocols have been reported to fabricate Au-Cu alloy structures with well-controlled shapes. For example, Li and coworkers[76] have synthesized intermetallic (ordered) Au-Cu spherical particles using a seed mediated growth method followed by thermal annealing (TEM images shown in Figure 3a and b). To form Au-Cu particles, homogeneous collision of Cu atoms or clusters occurred on the preformed Au seed surface at the initial stages of the growth, followed by diffusion of Cu atoms into the Au lattice. The nanoparticles were then annealed at elevated temperatures to form ordered Au-Cu alloy. Temperature required for annealing varied with the desired composition of final product (AuCu to $AuCu_3$). Seed mediated strategy was also extended to fabricate nanorods with different aspect ratios, which were difficult to achieve using the co-reduction methods. Sonnichsen and coworkers[77] fabricated Au-Cu alloy nanorods in aqueous phase using a seed mediated strategy.

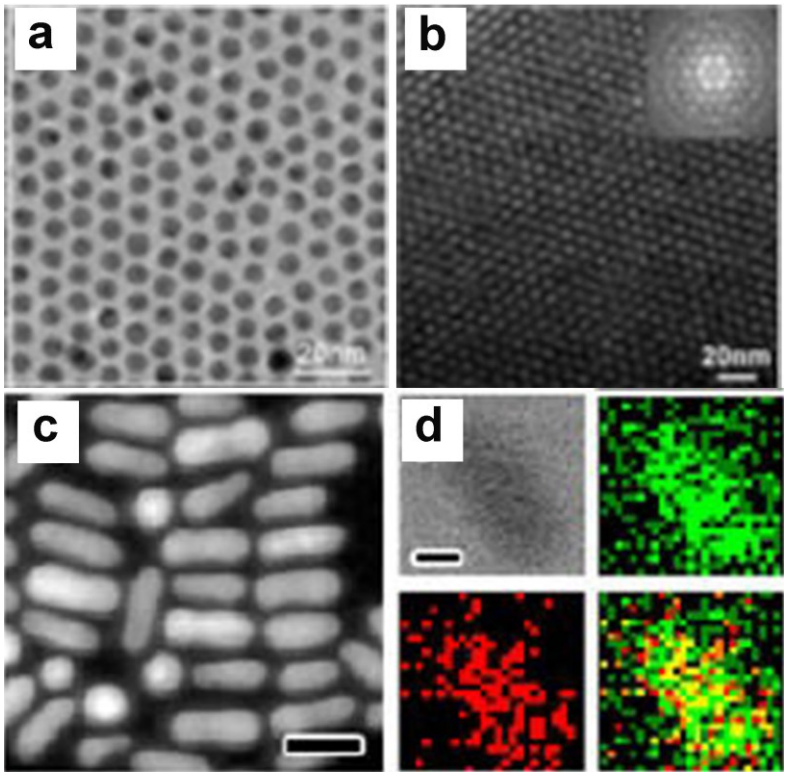


Figure 3. (a)TEM images of the intermetallic Au-Cu nanoaprticles. (b)TEM image of a multilayer hcp superlattice consisting of (6.0 0.2) nm CuAu NCs; inset shows the corresponding fast Fourier transform (FFT) pattern. (C) HAADF-STEM image of rods. (d) EDX mapping of samples in (C) with four panels: bright-field image, mapping of Cu (green), mapping of Au (red), and their overlaid image. The scale bars in the HAADF-STEM images are 20 nm while the scale bars in the bright-field images of EDX mapping are 5 nm. (a, b)Reproduced from reference 76, with permission from Wiley-VCH Verlag GmbH & Co. KGaA, Weinheim, Copyright 2010. (c, d) Reproduced from reference 79, with permission from American Chemical Society, Copyright 2013.

In their method, ascorbic acid was used as a mild reducing agent to reduce the copper precursor to Cu atoms. While cetyl trimethylammonium bromide (CTAB) was used as the ligands to promote the growth of Au-Cu nanorods along a specific direction on the Au seeds, similar to the method used to produce Au nanorods.[78] Later in 2013, Chen and coworkers[79] developed an organic phase seed mediated protocol for the synthesis of $AuCu_3$ alloy nanorods using Au nanoparticles as seeds, as shown in Figure 3c and d. In this protocol, oleylamine acted as both the solvent and mild reducing agent. The reduction rate of Cu was slow due to mild reducing

nature of olelyamine, favoring asymmetric addition of Cu atoms to the Au seeds. Later, our group confirmed the growth mechanism in a detailed study on Au-Cu alloy nanorods growth.[80] The intermediates at different stages of reaction were separated and analyzed, indicating Cu attachment on one side of Au seed, followed by inter diffusion of Cu into Au phase, forming Au-Cu alloy nanorods. Prospectively, heterogeneous nucleation (seed-mediated growth) requires less amount of reactants than co-reduction, and this strategy provides more possibility to fabricate many complex morphologies of Au-Cu alloy structures.

### *3.3 Combined Co-reduction and Seed-mediated Strategy*

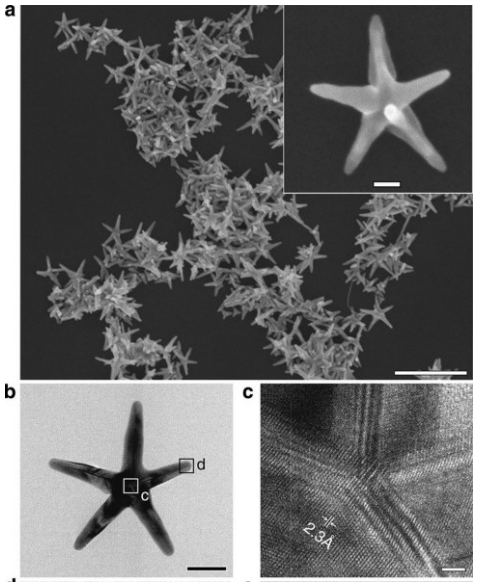


Figure 4. (**a**) SEM image of the pentacle nanocrystals prepared through the standard procedure. (**b**) TEM image of an individual pentacle Au–Cu alloy nanocrystal. (**c**) HRTEM images of the parts marked in **b**. Scale bar, 500 nm (**a**) and 50 nm (**b**). 2 nm (**c**). Reproduced from reference 81, with permission from Nature Publishing Group, Copyright 2014.

Co-reduction and seed mediated strategies can be combined to produce complex structures with sharp tips. The complex structures can be generated because the preformed Au seeds have certain surface sites (or facets) more reactive than the others. The further growth of Au-Cu crystals tends to occur on these reactive sites, creating sharp edges or branches along specific directions. Using co-reduction combined with seed mediated growth, Au-Cu alloy nanopentacles were fabricated by Hou and coworkers[81] as shown in Figure 4. In this work, glucose acts as a strong reducing agent and helps the formation of penta-twinned Au seeds. The twin boundaries can be

clearly seen in Figure 4c. Hexadecylamine functions as the ligand to selective bind to the (110) facets of the seed, favoring the addition of co-reduced Au and Cu atoms along the twinning planes of the Au seed. This selective growth accompanied by slow kinetics (caused by decrease in glucose concentration) results in the formation of branches and the final pentacle particles. Furthermore, the composition of nanopentacles can be tuned by varying the precursor to reducing agent ratio. The nanopentacles with sharp tips and high surface area are potentially good for catalytic and sensing applications. This work demonstrated that exquisite control of the morphologies and compositions Au-Cu alloy structures of can be achieved by combining the proper bottom up synthetic strategies.

### *3.4 Galvanic Replacement*

In the recent years, galvanic replacement reaction (GRR) has evolved as an efficient post modification strategy to produce bimetallic nanoparticles, alternative to the direct synthesis as mentioned above. In a typical GRR, monometallic nanoparticles of a certain composition and morphology will be fabricated first, and used as the templates. Another metal precursor of a higher reduction potential will be added to the templates, partially replaces the original metal atoms in the templates resulting in bimetallic particles. By varying the morphology of the templates and concentration of the metal precursors etc., bimetallic nanoparticles of sophisticated morphologies such as hollow nanocubes[82] and nanoshells[83] can be produced. Hollow structures achieved by GRR potentially have high catalytic activity because of their high surface-to-volume ratio. Thus, the post treatment using GRR can mitigate the inherent difficulties associated with the shape control in the direct synthesis of bimetallic nanoparticle.

Recently, Au-Cu alloy structures were explored as GRR templates. The alloy nature of the

templates gives rise to interesting structural and compositional changes during GRR. For example, our group used Au-Cu alloy nanorods as a bimetallic nanoparticle template for GRR with $HAuCl_4$ as the oxidizing agent.[84] We demonstrated that by manipulating oxidation rates with respect to diffusion, morphologies of the final products could be varied during GRR.[85] By simply changing the amount of $HAuCl_4$ precursor added to the reaction mixture, oxidation rates were varied. When low $HAuCl_4$ precursor concentration was used, Au-Cu alloy nanorods

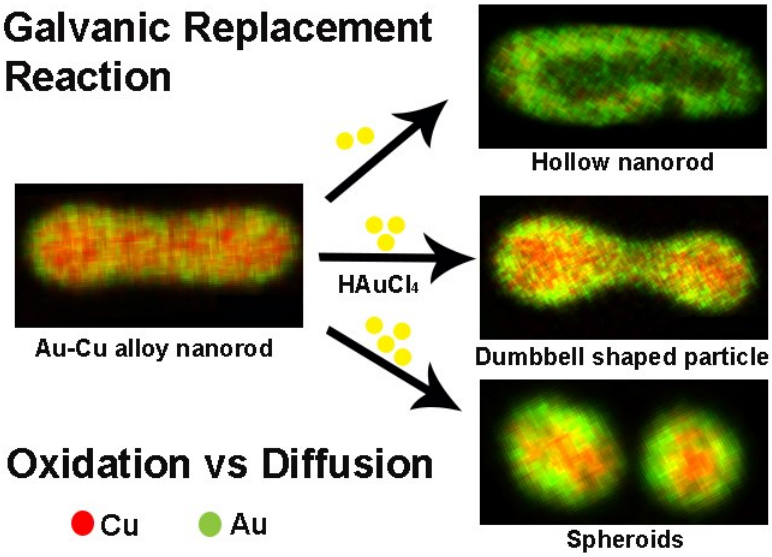


Figure 5. Scheme showing different products obtained due to GRR on Au-Cu alloy nanorods. For example when low $HAuCl_4$ concentration was used, hollow rods were formed. While at high $HAuCl_4$ concentrations, rod broke into alloy particles. At intermediate $HAuCl_4$ concentrations, dumbbell shaped particles were formed. Reproduced from reference 85, with permission from Royal Society of Chemistry, Copyright 2017.

transformed into alloy hollow rods (Figure 5, upper right image). Au-Cu alloy nanorods broke at the center and transformed into AuCu@Au spheroids when high concentration of $HAuCl_4$ precursor was used (Figure 5, bottom right image). The breaking of the nanorod involved formation of an asymmetric dumbbell shape intermediate state with a hollow junction in the middle (Figure 5, middle image on the right). Together with diffusion, dealloying played a crucial role in manipulating reaction pathways in these processes. Similarly, Wang and co-

workers[86] examined the effect of dealloying in Au-Cu alloy structures to create spongy alloy nanoframes. In their study, Cu was selectively leached using etchants like $Fe(NO_3)_3$, $HNO_3$. Percolation dealloying was observed in Au-Cu alloy structures with Cu content above a parting limit. Dealloying was also accompanied by nanoscale migration of atoms and atomic dissolution, resulting in spongy nanoframes. Ligament domain coarsening controlled by thermodynamics and framework expansion controlled by Kirkendall effect dictated the nanoporosity of the final product in this study. Nanoporosity controlled the catalytic activity of the spongy nanoframes. Overall, GRR in Au-Cu alloy structures indicated that manipulation of key factors like oxidation kinetics with respect to diffusion and dealloying could create novel morphologies with unique compositions, which are impossible to achieve through regular synthetic methods.

### *3.5 Decomposition of Single Source Precursors*

Single source precursors such as double complex salts have been used to obtain alloy nanoparticles on solid support films, which are often used for catalysis applications.[87-89] Double complex salts are coordination compounds consisted of complex cation and anion of two different metals. Decomposing the salt on the support surface or inside the support pore space is a convenient method to create heterogeneous catalysts. By adjusting the decomposition conditions, composition and morphology of the resulting nanoparticles can be adjusted. For example, Sobyanin and coworkers[90] have synthesized Au-Cu nanoparticles on $Al_2O_3$, $SiO_2$, $CeO_2$ support. Double complex salt $[Au(en)_2]_2$ $[Cu(C_2O_4)_2]_3 \cdot 8H_2O$ (where en - $H_2NCH_2CH_2NH_2$) was used as a single source precursor for both Au and Cu. The composition of the alloy particles obtained in this work varied between $Au_{0.4}Cu_{0.6}$ to $Au_{0.6}Cu_{0.4}$, with particle sizes around 5-10 nm. Similarly, bimetallic nanoclusters can also be used as single source precursors to synthesize alloy nanoparticles.[62, 91, 92] So far, Au-Cu nanoparticles fabricated from single precursor sources

are only obtained on support films. The composition of final product can be controlled precisely, but the size and shape control still poses a lot of challenges. The uniformity of the nanoparticles obtained using the decomposition method needs to be improved to enhance their catalytic performance. Decomposition of single source precursors is an interesting method to fabricate Au-Cu nanoparticles, which demands a lot of future work to optimize the synthesis and extend the method to fabricate nanoparticles without support films.

### *3.6 Summary of the Common Synthetic Methods*

In the table below, we summarized the common synthetic methods to produce Au-Cu nanoparticles that have been developed so far. The table can be used as a reference for future synthetic design of Au-Cu nanostructures with desired size, shape, and composition for a wide range of applications.

| Sample | Composition (Au:Cu ratio) | Shape | Size | Methods | Reference |
|---|---|---|---|---|---|
| **$Au_{1-x}Cu_x$ nanoparticles** | 1.43-24 | Spherical | 8-12 nm | Co-reduction | [73] |
| **AuCu Dimetallic Nanowire** | 1:1 | Nanowires | 3.7 nm | Co-reduction | [74] |
| **Au-Cu Nanocubes** | 1:3- 3:1 | Nanocubes | 3.4-85 nm | Co-reduction | [75] |
| **CuAu and $Cu_3Au$ Nanocrystals** | 1:1, 1:3 | Spherical | 10-11 nm | Seed-mediated growth | [76] |

| | | | | | |
|---|---|---|---|---|---|
| **$Au_xCu_{(1-x)}$ nanoparticles** | 4:1- 1:4 | Nanorods | 20-40 nm | Seed-mediated growth | [77] |
| **CuAu bimetallic nanorods** | 1:3 | Nanorods | 25.2 * 8.5nm | Seed-mediated growth | [79] |
| **Pentacle Au-Cu alloy nanocrystals** | 6.93 | Pentacles | 10–40 nm in width and 80–150 nm in length | Combined Co-reduction and Seed-mediated Strategy | [81] |
| **Hollow Au–Cu alloy nanorods** | - | Hollow nanorods | 34.2 nm | Galvanic replacement | [84] |
| **Spongy $Au_{0.97}Cu_{0.03}$ nanoframes** | 32.33 | Spongy nanoframes | 120 nm | Dealloying | [86] |
| **AuCu/ $\gamma$ -$Al_2O_3$** | 0.87 | Nanoparticles on support surface | 10-15 nm | Single source precursors | [90] |
| **AuCu bimetallic nanoparticles** | 1:1 | Spherical | 6 nm | Seed-mediated growth | [93] |
| **AuCu intermetallic nanoparticles** | 1.3 | Spherical | 7.8 nm | Co-reduction | [94] |
| **Au-Cu nanocubes** | 0.43, 3.29 | Cubic in-plane | 22.9 nm | Co-reduction | [95] |

| | | | | | |
|---|---|---|---|---|---|
| **Au-Cu nanoalloys** | 4, 0.37 | Small dots | 1.7 nm, 1.9 nm | Pulsed Laser deposition | [95] |
| **Au-Cu bimetallic nanoparticles** | 3:1, 1:1, 1:3 | Spherical | 10-11 nm | Co-reduction | [96] |
| **AuCu alloy nanoparticles** | 3:1- 1:5 | Nanocubes | 2-6 nm | Thermal Evolution | [62] |

Table 1. Summary of Au-Cu alloy sample name, composition, geometry, size and synthetic method.

Among all the above-mentioned synthetic methods, co-reduction is the most direct and well-developed strategy, yielding a large variety of Au-Cu nanoparticles. In co-reduction method, a general requirement is that the reduction potentials of the two metal precursors have to be close. However, for Au-Cu system, the reduction potential of $Au^{3+}$ (+1.50 V) and $Cu^{2+}$ (+0.34 V) are not close enough. In order to produce Au-Cu nanoparticles with co-reduction method, the reduction of the two precursors needs to be synchronized. Consideration should be given to coordination ligands and the molar ratio of the precursors, which can regulate the reduction rates of the precursors. To control the shape of the Au-Cu nanoparticles, special capping agents (e.g. $Ag^{+}$, $Cu^{2+}$, CTAB, polymers and biomolecules) can be introduced to selectively bind to specific facets of the nanocrystal to increase or decrease the growth rate along these facets, therefore, leads to anisotropic structures[9]. Generally speaking, co-reduction is the most versatile method to synthesize simple structure (spherical, cubic) with high yield in a simple step.

What seed-mediated growth provides to us is better consistency and reproducibility from batch-to-batch. In seed-mediated growth, size, shape and concentration of the seeds shall be determined before using them in the growth, typically by electron microscopy and inductively-coupled plasma mass spectrometry. Quantitatively controlling the ratio of the seeds to the amount of precursor is crucial in the further synthesis of both isotropic (e.g different composition and atomic ordering in AuCu nanoparticles[76]) and anisotropic structures (e.g. different aspect ratio[77] and different composition[79] in AuCu nanorods). Twinned planes of the pre-synthesized seeds also have an impact on anisotropic nanoparticle synthesis[97], and is an interesting factor on AuCu nanoparticle synthesis to be investigated in the near future. If good geometry control or special structures of nanoparticles are desired (such Au-Cu nanorods), seed-mediated growth can be firstly considered.

Galvanic replacement brings the possibility of synthesizing hollow Au-Cu nanostructures with finely tuned external and internal structure. This unique electrochemistry process is very sensitive to reaction conditions. In galvanic replacement reactions, concentrations of the template and the metal precursors should be chosen carefully which will affect the reduction potential and galvanic replacement rate. Temperature and strain effect also need to be considered which have an impact on the diffusion of atoms that often occurs along with galvanic replacement. The diffusion of atoms can make the composition of the body and surface of the nanoparticles different, leading to challenge in the composition control of the product. The hollow nanostructures fabricated by galvanic replacement reactions have high surface area to mass ratio, which is highly desired for catalytic applications. However, special consideration should be given to the reaction conditions in order to obtained nanoparticles with well-controlled morphology. A drawback of galvanic replacement reaction is that the reaction yield is typically

much lower than co-reduction and seed-mediated growth methods, which needs to be improved in the future research.

## 4. Optical properties

### *4.1 Effect of Geometry, Size and Composition on the Localized Surface Plasmon Resonance (LSPR)*

The loosely bound electrons in metal nanoparticles oscillate collectively when exposed to external electromagnetic radiation. If the oscillation frequency matches with that of the external source, resonance occurs, giving rise to localized surface plasmon resonance (LSPR). [4, 98, 99] The frequency, at which the resonance happens, depends on composition and morphology of the nanoparticles, and also the dielectric constant of the medium, and. Both Au and Cu nanoparticles are active plasmonic materials with LSPR in the visible wavelength region. For example, 20 nm spherical Au and Cu nanoparticles display LSPR at 520 and 560 nm, respectively.[100] But Cu nanoparticles can easily get oxidized to copper oxides, quenching their LSPR[47]. Alloying Cu with chemically more inert Au prevents the oxidation of Cu and the optical properties of the alloy nanoparticles are different from that of the Au or Cu nanoparticles.

LSPR wavelength and line shape of Au-Cu alloy particles depend on not only their size and shape, but also the alloy composition. Typically, alloying of Cu into Au nanoparticles causes a red shift and broadening of LSPR, as shown in Figure 6. For example, spherical $Au_xCu_{1-x}$ (x= 0 to 0.5) alloy nanoparticles of sizes 8-13 nm display a single peak in the visible region.[73] A red shift from 523 nm to 545 nm was observed when Cu content was increased from 0 to 48 %. Similar results were observed by Yang and co-workers (Figure 6a).[96] When the composition of the nanoparticles was varied from $Au_3Cu$ to $AuCu_3$, the LSPR peak red shifted from 530 to 570

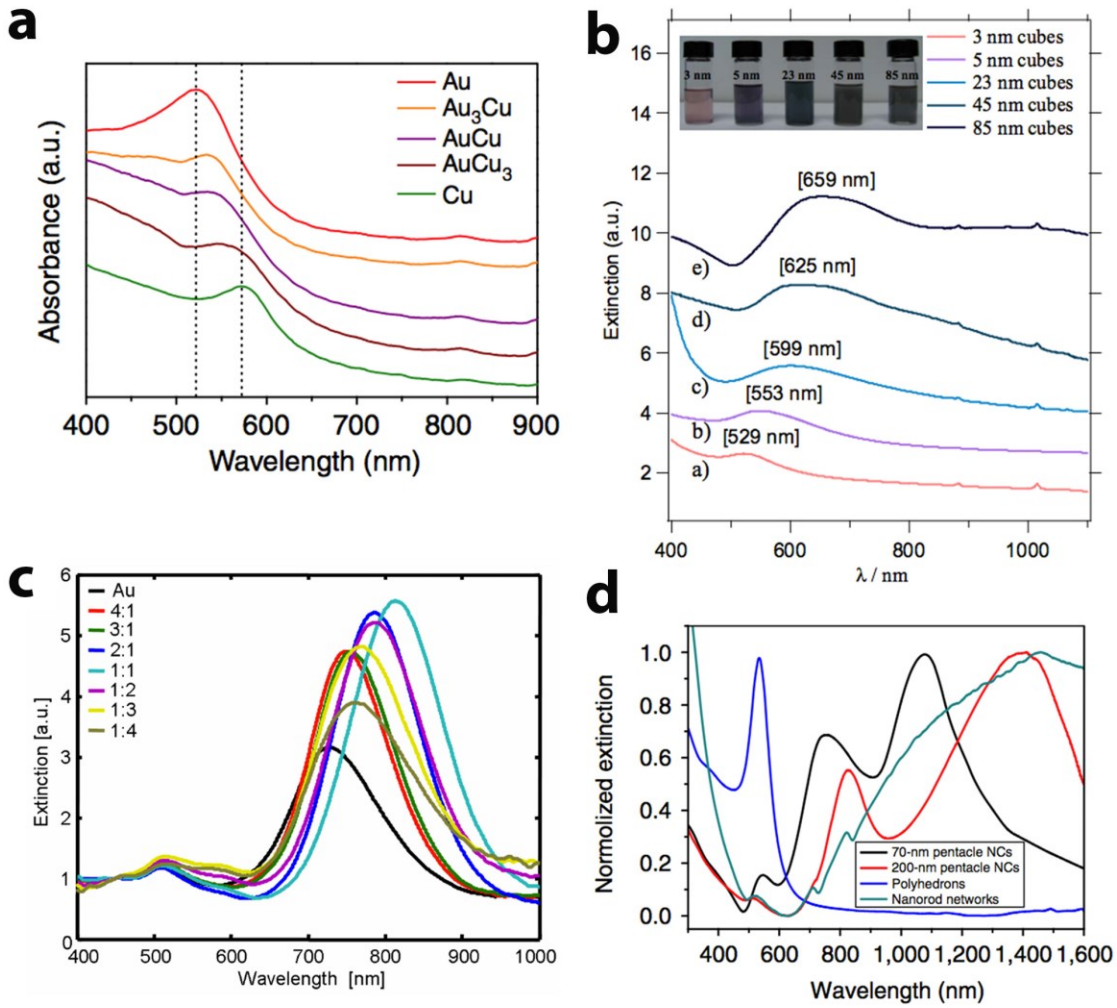


Figure 6. Extinction spectra of Au-Cu alloy nanoparticles of different shapes. (a) Nanospheres (b) Nanocubes (c) Nanorods (d) Nanopentacles. Spherical particles and cubes display a single peak in the spectra, while rods have two peaks and nanopentacles have multiple peaks. (a) Reproduced from reference 96, with permission from Nature Publishing Group, Copyright 2014. (b) Reproduced from reference 75, with permission from Wiley-VCH Verlag GmbH & Co. KGaA, Weinheim, Copyright 2010. (c) Reproduced from reference 77, with permission from American Chemical Society, Copyright 2009. (d) Reproduced from reference 81, with permission from Nature Publishing Group, Copyright 2014.

nm. In both of these studies, the LSPR peak of Au-Cu alloy particles was between that of Au and Cu nanoparticles. In addition to alloy composition, the LSPR depends on size of the alloy nanoparticles as well. As shown in Figure 6b, the LSPR of the $AuCu_3$ alloy nanocubes red shifted from 529 to 659 nm when cube edge length was increased from 3 to 85 nm.[75] However,

the LSPR of the $AuCu_3$ nanocubes has only one broad peak. The expected higher order modes for the cube morphology were absent in the LSPR of Au-Cu alloy nanocubes, similar to that of the Au, Ag nanocubes.[101, 102] When the geometry of the nanoparticles becomes rod-like, two peaks were observed in the LSPR as shown in Figure 6c. The small peak at shorter wavelength is due to the transverse plasmon mode and the main peak at longer wavelength comes from the longitudinal plasmon mode.[77] This study has also shown that with the increase in the Cu content of the nanorods, the transverse mode becomes weaker. Similar phenomena were observed in other studies on $AuCu_3$ alloy nanorods, where the transverse mode was completely absent.[79, 80] In contrast, the longitudinal plasmon mode was strong and sensitive to the composition change of the nanorods. It red shifted from 720 nm to 820 nm when the Au: Cu ratio was changed from 4:1 to 1:1 , but then blue-shifted from 820 to 780 nm when the Cu content was further increased from 1:1 to 1:4 (Figure 6c). The LSPR of the Au-Cu alloy nanoparticles display multiple peaks when the morphology becomes more complex. For example, the LSPR of 70 nm Au-Cu alloy pentacle particles had three bands as shown in Figure 6d.[81] A major peak was found at 1100 nm, which is dipolar in nature, while two higher order modes were observed at 740 and 550 nm. Similarly, the LSPR of the 200 nm pentacles displayed three peaks at 1400, 810 and 530 nm (red curve in Figure 6d).

To summarize, Au-Cu alloy nanoparticles have LSPR bands in the visible-NIR wavelength region, which are sensitive to the geometry and composition of the nanoparticles. As the geometry changes from simple spherical shape to complex pentacle shape, multiple peaks appeared due to higher order plasmon modes. Furthermore, a common trend was observed for the Au-Cu nanoparticles of all morphologies, i. e., the LSPR red shift and broadens with the increase in Cu content of the nanoparticles. The broad LSPR bandwidth might be due to the

polydispersity of the samples or plasmon damping, which can be elucidated by single particle optical studies.

### *4.2 Structural Defects induced Plasmon Peak Splitting*

The LSPR of Au-Cu nanoparticles was found to be very sensitive to the structural defects, which are inevitable during the alloying process.[24, 103-105] The difference in lattice parameters between Au and Cu creates strain when alloy particles are synthesized. The lattice dissipates the strain by forming structural defects as observed in previous studies.[67, 106] In a recent study from our group, structural defects of a few atomic layers were observed during the synthesis of $AuCu_3$ alloy nanorods.[80] Single particle scattering studies performed on the intermediates during the growth of Au-Cu alloy nanorods revealed that the LSPR of the nanorods displayed multiple peak patterns, instead of a single peak as observed in the bulk solution of Au-Cu alloy nanorods. Discrete dipole approximation (DDA) simulations revealed that the multiple peaks were caused by structural defects in the rod shaped intermediates as shown in Figure 7. When one trench like defect of 0.5 nm width and 1.25 nm height was induced in the nanorod (Figure 7C), the LSPR

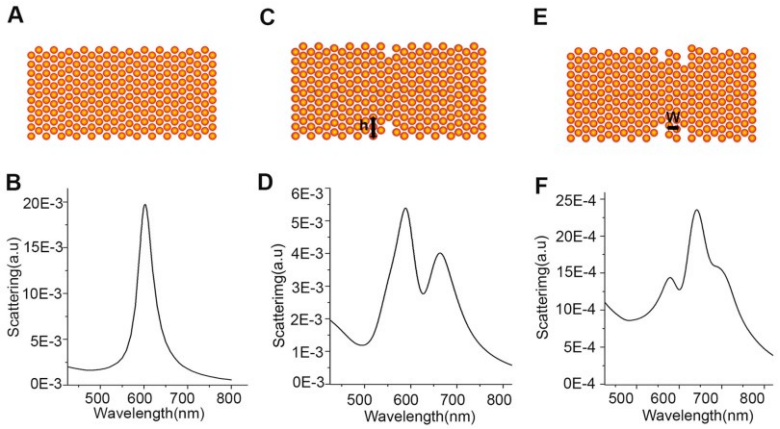


Figure 7. Schemes (A, C and E) and calculated scattering spectra (B, D, and F) of an Au-Cu alloy rod without and with defects. (A-B) Scheme and corresponding scattering spectrum of a rod without defect. (C-D) Scheme and corresponding scattering spectrum of a rod with one well-like defect where the width of the defect is 0.5 nm and the height (h) is 1.25 nm. (E-F) Scheme and corresponding scattering spectrum of a rod with two well-like defects where the defects are 1.5 nm and 1.0 nm in height, and 0.5 nm in width. The defects are separated by a distance (w) of 1.0 nm. Reproduced from reference 80, with permission from Royal Chemical Society, Copyright 2015.

displayed two peaks (Figure 7D). The DDA simulations revealed that, rod was separated into two halves by the defect and the interaction between two halves gave rise to the higher order plasmon modes. Also, when additional defects were added as shown in Figure 7E, the LSPR displayed multiple peaks (see Figure 7F). The studies show the sensitivity of LSPR towards structural defects of a few atomic layers in alloy nanoparticles.

### *4.3 Plasmon Damping*

Under LSPR excitation, free electrons of metal oscillate at the plasma frequency until the energy is consumed by a process called plasmon damping. Plasmon damping in Au-Cu alloy samples was not explored much and very few examples are known till today. In one study, plasmon damping effect was studied by examining the Au-Cu nanorods scattering peak width using single particle dark field scattering spectroscopy.[77] The study revealed that plasmon damping in the Au-Cu samples was mainly due to the intra band transition of Cu or Au-Cu alloy i.e. electron-electron collisions in the lattice. The damping effect was dependent on Cu content in the alloy nanoparticles. For example, plasmon damping is lower for samples with a Au:Cu ratio of 4:1, 2:1, 1:2 and 1:4 compared to those of 3:1, 1:1 and 1:3. We speculate that plasmon damping may lead to the broadness of the LSPR of Au-Cu nanocubes and might have caused the quenching of the higher order modes. Similarly, plasmon damping may have resulted in the weakening of the transverse mode in the LSPR of the Au-Cu nanorods. But mores studies need to be performed in order to confirm this effect. The unique optical features and plasmon damping of alloy Au-Cu structures of different morphologies further need to be explored with the aid of single particle experiments combined with theoretical calculations.

## 5. Applications

## 5.1 Catalytic Applications

### *5.1.1 $CO_2$ Reduction*

Electrochemical reduction of carbon dioxide into chemical fuels not only reduces $CO_2$ emissions but also decreases the usage of non-renewable fossil fuels.[107] However, it is very challenging to efficiently reduce $CO_2$ due to the complexity of the process.[108] Large over potentials are required to reduce $CO_2$ when using different metal electrodes like Cu (most used),[109, 110] Sn[111] and Au[112], which leads to undesired reactions instead of $CO_2$ reduction [108, 113, 114]Large over potential also means large amount of energy is required for the electrochemical reduction of $CO_2$. To overcome this problem, metal alloy nanoparticles have been exploited as the catalysts. In particular, alloying Au with Cu reduces the over potential required for $CO_2$ reduction and stabilizes Cu. [45] In addition to the over potential, selectivity of the catalysts needs to be considered for $CO_2$ reduction because multiple proton and electron coupling steps are involved in the process, which results in many possible reaction products like methane, ethylene, carbon monoxide, formate and hydrogen. Yang and co-workers[96] demonstrated that Au-Cu alloy nanoparticles are highly efficient catalysts for $CO_2$ reduction. The catalytic activity and selectivity can be tuned by the composition of the Au-Cu alloy. In this study, Au-Cu nanoparticles were self-assembled to form a monolayer of nanoparticles for $CO_2$ reduction. By tuning the Au to Cu ratio, different final products were observed.

The selectivity of the catalysts towards different products was ascribed to the electronic and geometric effects, which selectively stabilized certain reaction intermediates on catalytic surface. Specifically, increasing Au content in the alloy nanoparticles increased the faradaic efficacies for methane, ethylene and hydrogen while opposite trend was observed for carbon monoxide. $Au_3Cu$, $Au_3Cu$, AuCu and $AuCu_3$ nanoparticles demonstrated 93.1, 83.7 and 40.4 times of the

turnover rates for CO compared to Cu nanoparticles as shown in Figure 8a. $Au_3Cu$ nanoparticles also have the best mass activity for CO (see Figure 8b). Optimizing the binding strength of desired intermediate species like CO was the key in enhancing the selectivity and activity for $CO_2$ reduction. The studies have shown that alloying of Au to Cu reduced the over potential for the $CO_2$ reduction, and at the same time increased the selectivity and stability of the catalysts.

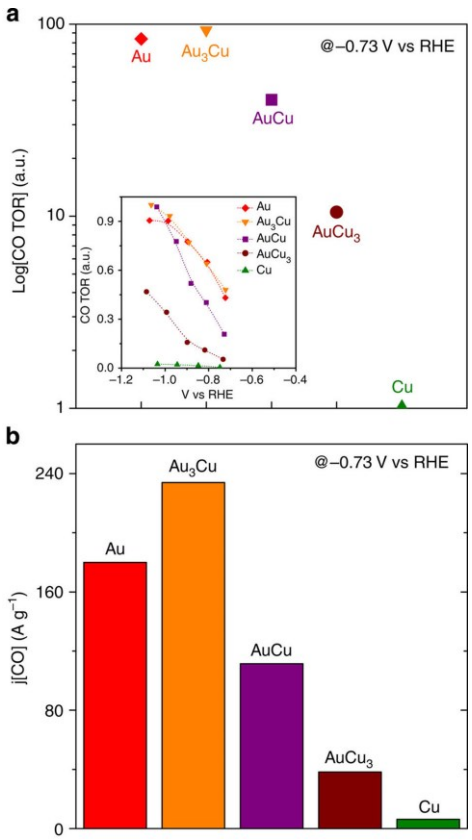


Figure 8. (a) Relative turnover rates for CO and (b) CO mass activity. Reproduced from reference 96, with permission from Nature Publishing Group, Copyright 2014.

### *5.1.2 P-nitrophenol reduction*

P-nitrophenol is a toxic byproduct formed during the production of synthetic dyes, herbicides and pesticides.[115, 116] It can be converted to non-toxic products like *p*-amino phenol using reducing agents like $NaBH_4$.[117, 118] Due to the ease of tracking the kinetics of this reaction by simply following the absorbance of the *p*-nitrophenol, it has been used as a model reaction over the years to study the catalytic activity.[115, 119-122] Au-Cu alloy particles of various shapes have been demonstrated as excellent catalysts for this reaction due to the electronic and geometric effects.[123] The electronic structure (d-band center) of Au-Cu alloy particles can be adjusted by tuning their composition to achieve optimal adsorption of the reactants and intermediates.[124, 125] In addition, the shape and internal structures of the nanoparticles can be varied using different synthetic schemes to further enhance their catalytic

activity due to geometric effects. Au-Cu alloy nanoparticles of various morphologies like spheres, rods, hollow rods and pentacles were explored as catalysts for *p*-nitrophenol reduction.[67,69,70] In a comparative study[79] between $AuCu_3$ nanoparticles and nanorods, nanorods demonstrated higher activity than the nanoparticles, due to presence of high index facets. Interestingly in the same study, the nanoparticles of same shape with different crystal phases showed different catalytic activity. The ordered phase showed twice the catalytic activity as the disordered phase. Considering the shape and crystal phase, the ordered nanorods demonstrated the highest catalytic activity for *p*-nitrophenol reduction in this work. Later, our group showed that hollow Au-Cu alloy rods exhibited enhanced catalytic activity compared to the solid alloy nanorods.[84] The apparent rate constant normalized to the surface area, was 5 times higher for the hollow alloy nanorods compared than that of the solid alloy nanorods. The high catalytic efficiency was attributed to the Au-Cu alloy composition, specific crystal facets, hollow internal structure and high number of Au atoms exposed on the surface. In addition to alloy nanoparticles and

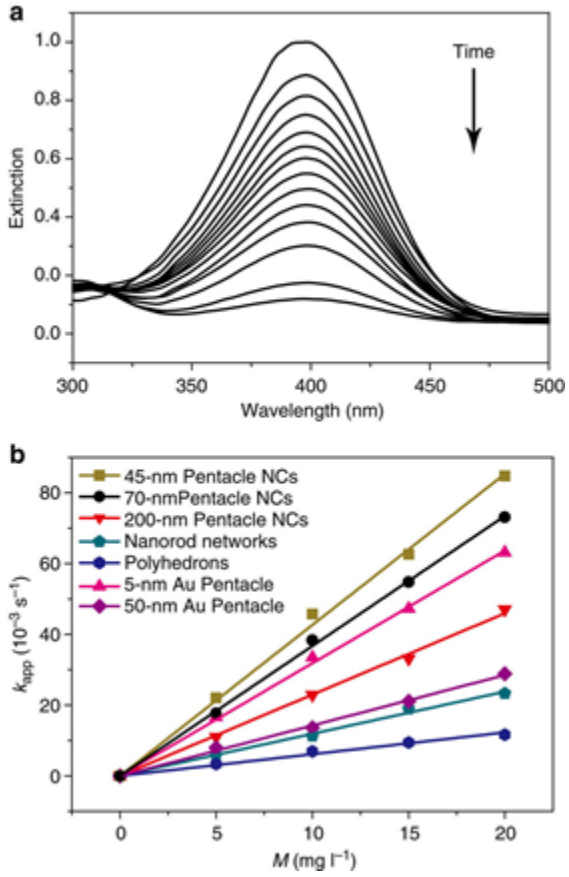


Figure 9. (**a**) The extinction spectra recorded at different reaction time points, indicating the disappearance of the peak for p-nitrophenol. (**b**) Plots of the apparent rate constants (kapp) as a function of the mass concentration (M), relating to the use of different types of Au–Cu bimetallic nanocrystals and Au nanoparticles as catalysts. Reproduced from reference 81, with permission from Nature Publishing Group, Copyright 2014.

nanorods, nanopentacles were also used for p-nitrophenol reduction.[81] In this work, the nanopentacles demonstrated higher catalytic activity compared to Au-Cu nanorod networks and polyhedrons (Figure 9) because nanopentacles enjoyed large surface areas provided by the branches, and also high index facets and twinning interfaces. Alloy nanopentacles of three different sizes (45, 70 and 200 nm) were compared to study the size effect on their catalytic activity. 45 nm pentacles demonstrated highest catalytic activity compared to the other two sizes. Both 45 and 70 nm nanopentacles showed higher catalytic activity compared to 5 nm Au pentacles even their sizes were much larger. This shows that the alloy composition and high index facets and branches of the Au-Cu nanopentacles are the major reasons leading to the improved catalytic activity, despite their surface area/volume is smaller than the 5 nm Au pentacles.

Apart from the structural features of the Au-Cu alloy nanoparticles, the synergism resulted from alloy composition is the major contributing factor for the increased catalytic activity. As explained by the volcanic plots, Au-Cu composition has optimum catalyst- adsorbate binding energy required for adsorption and desorption of *p*-nitrophenol, compared to pure Au and Cu atoms. The alloying of Au (with a large lattice constant) with Cu (with a smaller lattice constant) causes lattice compression, leading to increased overlap of orbitals. This effect makes the d-band center to shift away from the Fermi level, generating the optimum adsorption energy for *p*-nitrophenol reduction.[115, 126] Therefore, the reaction rate constants for AuCu alloy nanoparticles is increased compared to that for Au and Cu nanostructures.

### *5.1.3 Methanol and CO Oxidations*

Au-Cu alloy nanoparticles were also explored as catalysts for other reactions like methanol oxidation reaction (MOR) and CO oxidation. Wang and coworkers[86] showed that Au-Cu alloy spongy nanoframes exhibited an order of magnitude higher electrocatalytic activity compared to surface roughened Au nanoparticles and multifaceted quasi-spherical Au nanoparticles of same size. The spongy nanoframes also exhibited 3 and 5 times better mass activities compared to Au bowls and Au shells for MOR. This superior catalytic activity of the nanoframes was attributed to the high densities of surface active sites, and uncoordinated surface atoms.

Au-Cu alloy systems supported on different materials like $SiO_2$, $TiO_2$, SBA-15, and carbon were explored as catalysts for CO oxidation.[52, 62, 127, 128] Generally, Au (0) is believed to be the active site for CO oxidation due to its strong affinity to CO revealed by infrared spectroscopy. Meanwhile, Cu (0) plays an important role in activating oxygen. However, Au-Cu nanoparticles alone are not catalytically active for CO oxidation in its original form. The formation Au-$CuO_x$ structure has been found to be essential to catalyze this reaction. Liu and coworkers[128] suggested that the $Cu^0$ component was enriched on the surface of the alloy nanoparticles under CO oxidation condition and form tiny patches of $CuO_x$ that can provide active $O^{\delta-}$ species. Zhan and coworkers[129] have also pointed out that the thickness of $CuO_x$ on the surface is also crucial because thick $CuO_x$ layer will prevent CO and $O_2$ from approaching active sites and slow down activation. Size, shape and composition effects on the catalytic activity of Au-Cu nanoparticles for CO oxidation have also been investigated. [102-104] In addition, Zhan et al.[129] have examined the role of the crystal structure of Au-Cu supported on $TiO_2$ for CO oxidation. They observed that oxidized face centered tetragonal (*fct)* Au-Cu nanocrystals had higher catalytic activity compared to oxidized face centered cubic (*fcc)* nanocrystals, because of lower CO and $O_2$ adsorption energies on *fct* Au-Cu compared to *fcc* Au-Cu.

The work discussed above have shown that Au-Cu alloy nanoparticles are promising catalysts for many important chemical/electrochemical reactions. The size, composition, morphology and crystal facets of the nanoparticles are critical factors that determine their catalytic activities. The support of the catalysts also play an important role, and it has been discussed elsewhere[27].

### *5.1.4 Photocatalytic reaction*

Hybrid metal and semiconductor nanostructures have raised high interest in photocatalytic reactions lately. Semiconductors are important for energy substitution and environment governance, because they can serve as photocatalyst for reactions such as hydrogen production reaction[130, 131] and $CO_2$ reduction[132]. However, due to the weak visible absorption and low catalytic efficiency of many semiconductor catalysts, semiconductor comes short of being an ideal catalyst. Plasmonic metals with high photon absorption efficiency are introduced to solve these problems. The LSPR of many metal nanoparticles can be efficiently excited with visible light. Direct energy transfer (DET), resonant energy transfer (RET), (hot) electron transfer (Figure 10a) or local electromagnetic field enhancement allows the electrons/energy to be transferred between semiconductors and metals[133]. These physical processes increase the charge separation and decelerate the recombination of the charge carriers in the semiconductor and therefore improve their photocatalytic performance. Au-Cu bimetallic nanoparticles perfectly fit in this role as they show tunable LSPR absorption in the visible wavelength region. More importantly, the synergistic effect between Au and Cu shows promise in further increasing the electron transfer efficiency in the system, better than the monometallic particles.

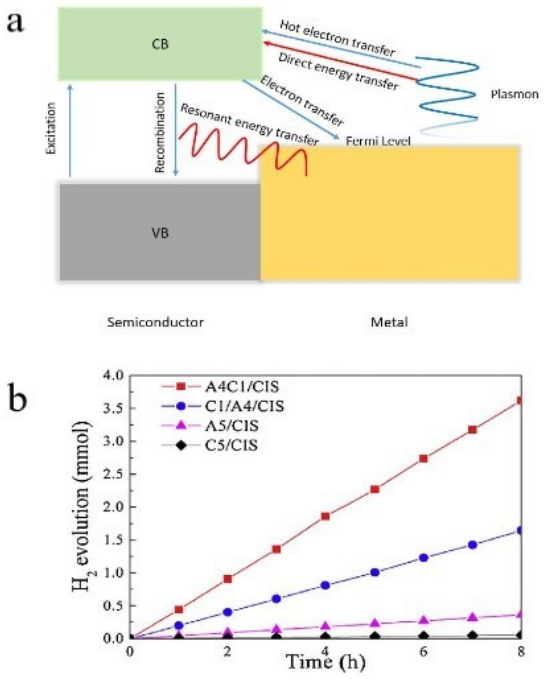


Figure 10. (**a**) Scheme of electron transfer and energy transfer between semiconductor and metal (**b**) Catalytic performance of $Au_{0.4}Cu_{0.1}/CaIn_2S_4$, $Cu_{0.1}/Au_{0.4}/CaIn_2S_4$, $Au_{0.5}/CaIn_2S_4$, $Cu_{0.5}/CaIn_2S_4$ in $H_2$ evolution reaction. Reproduced from reference 129, with permission from Elsevier, Copyright 2018.

Recently, Ding and coworkers[130] used a site-selective photo-deposition method to obtain Au-Cu alloy nanoparticles/$CaIn_2S_4$ , AuCu core-shell nanoparticles/$CaIn_2S_4$ , Au nanoparticles/$CaIn_2S_4$ and Cu nanoparticles/$CaIn_2S_4$ composites. The weight percentage of the nanoparticles was kept to be 0.5% of the weight of total composite. Alloyed $Au_{0.4}Cu_{0.1}/CaIn_2S_4$ composite exhibited the highest activity with a hydrogen production rate of 452.8 μmol/h, which was 2.2, 10.0, 63.8 and 76.7 times higher than that of the core-shell $Cu_{0.1}/Au_{0.4}/CaIn_2S_4$, monometallic $Au_{0.5}/CaIn_2S_4$, monometallic $Cu_{0.5}/CaIn_2S_4$ and $CaIn_2S_4$ alone, respectively (Figure 10b). Although the mechanism underlying the improvement on the photocatalytic performance is not clear, this result shows that a drastic increase on photocatalytic properties can be achieved by tuning composition and geometry of the alloy nanoparticles.

### 5.2 Photothermal Applications

Photo thermal therapy using plasmonic nanoparticles is a very important application of nanotechnology in medicine.[134] Out of all plasmonic materials, Au nanoparticles have been

mostly studied for photo thermal properties due to their biocompatibility, easy surface modification and well-developed synthetic protocols.[135-137] Recently, pentacle Au-Cu alloy system was explored for photothermal therapy. In this study[81] both 70 and 200 nm Au-Cu alloy nanopentacles were injected to mice tumor cells, and then irradiated with NIR laser. It was found that nearly 90 % of the tumor cells were killed after 10 min of irradiation and exposure to the nanopentacles. The tumor volumes were also reduced significantly compared with tumor samples with injection-only and radiation-only. Strong absorption in NIR and highly efficient photo thermal conversion were observed for 70 nm Au-Cu nanopentacles under an 808 nm laser irradiation, killing breast tumors in mice. This work demonstrates the potential application of Au-Cu alloy nanoparticles in tumor diagnostics and therapeutics.

## Summary and Future Outlook

In summary, Au-Cu alloy nanoparticles of well-controlled shapes were fabricated using various bottom-up synthetic approaches. Spheres, rods, wires, cubes and pentacles were among the different shapes that have been obtained so far. Ligands and Au/Cu stoichiometric ratios were determined to be the key factors for shape control in the Au-Cu alloy nanoparticle synthesis. Post synthesis modifications like GRR have also been used to form hollow rods, hollow junction dumbbell shaped particles and spongy nanoframes. The oxidation kinetics, dealloying, and Kirkendall effect played important roles in determining the morphology and composition of final products. Phase diagrams have also been introduced to understand phase segregation, favorable geometry and size, providing valuable information of synthesizing specific nanoalloys. The Au-Cu nanoparticles exhibit LSPR in the visible and NIR wavelength region. The LSPR wavelengths of Au-Cu alloy nanoparticles were typically between that of the Au and Cu nanoparticles of same size and shape, and highly composition, geometry and size-related. The

Au-Cu alloy nanoparticles had excellent catalytic activity owing to the geometric and electronic effects.

Currently, the studies of Au-Cu alloy systems are still limited in terms of synthesis and applications. Due to the inherent difference in the lattice constants and reduction potentials of Au and Cu, shape control is still challenging. Reproducibility of the synthesis is another limitation, as slight change in experimental conditions would vary the reaction kinetics and pathways drastically, especially for complex shapes. Post synthetic modifications like GRR can be further explored to create multimetallic nanoparticles from Au-Cu systems, by selectively replacing Cu with Ag, Pt, Pd, Rh etc. Especially, more studies are needed to understand the influence of crystal structure on GRR mechanism, for example ordered vs disordered alloy templates. Since the LSPR of alloy nanoparticles are not simply between that of the nanoparticles composed of the parent elements. More detailed studies on the optical properties of Au-Cu nanoparticles are required, especially for the complex shapes such as nanocubes. Theoretical methods based on electrodynamics simulations can greatly deepen the understanding of the fundamental optical properties of the alloy nanoparticles. However, the dielectric functions of the metal alloys with varying composition can be difficult to obtain, which is not necessarily a simple linear combination of the dielectric functions of the constituents. Some modeling is necessary to determine the proper dielectric functions.

In terms of catalytic applications, Au-Cu alloy nanoparticles of shapes other than spheres can be further explored. Catalytic rate is exponentially dependent on the adsorption energy between the active sites and reactants. Adsorption energy is determined by the composition, size and facet of the nanocrystals. In addition, ligands and the metal alloy may undergo a charge transfer process, tuning the surface electronic structure of the nanoparticles, and therefore affect their catalytic

activity[9]. Also, the influence of crystal structure and atomic ordering (intermetallic vs random alloy) on the catalytic activity of the nanoparticles worth's a lot of attention. It has been demonstrated that ordered Au-Cu alloy exhibited an enhanced catalytic properties on $CO_2$ reduction reaction[93]. However, the mechanism of how atomic ordering affects catalytic performance still remains to be studied. From the discussions in this review and many others, many factors have simultaneously influenced the catalytic performance of the nanoparticles (not limited to Au-Cu system, but true for all kinds of nanoparticles). Even at the nanoscale, the active sites for catalysis can vary from one particle to another. The criteria for a nanoparticle to be a good catalyst for one reaction are different from that for another reaction. With all these complicating factors, it still a grand challenge to establish a structure-property relationship that relates the nanoparticle structure to their catalytic performance and this relationship is being pursued and yet to achieved. Moreover, when metal components are attached on semiconductor nanocrystals, electron transfer from the semiconductor to the metal may happen, preventing quick electron-hole pair recombination. This process consequently improves the photo-catalytic performance of the semiconductor. Current research largely focuses on combining monometallic component with semiconductor nanocrystals. However, by tuning the composition of the metal such as using metal alloy instead of a single metal, their electronic density of states will be modulated, and therefore potentially affecting the charge transfer efficiency from the semiconductor to the metal, the hot electron transfer efficiency from the metal to the semiconductor, and other energy transfer processes[138, 139]. Hybrid metal alloy-semiconductor nanostructures opens up opportunity in further improving the photo-catalytic efficiency for a wide range of chemical reactions. In conjunction with catalytic measurements, ultrafast spectroscopy can be applied to determine the charge transfer rate and hot electron transfer

efficiency in the metal alloy/semiconductor structures, which will help to elucidate the photo-catalytic mechanism. The research presented in this review has laid the foundation for exciting future work on the Au-Cu alloy nano systems.

AUTHOR INFORMATION

**Corresponding Author**

*Email: jing.zhao@uconn.edu

**Funding Sources**

NSF CHE# 1554800

ACKNOWLEDGMENT

We would like to acknowledge the financial support from National Science Foundation CAREER AWARD (CHE# 1554800).

## References:


1. P. Chen, X. Zhou, N. M. Andoy, K.-S. Han, E. Choudhary, N. Zou, G. Chen and H. Shen, *Chemical Society Reviews*, 2014, **43**, 1107-1117.
2. V. Giannini, A. I. Fernández-Domínguez, S. C. Heck and S. A. Maier, *Chemical Reviews*, 2011, **111**, 3888-3912.
3. G. V. Hartland, *Chemical Reviews*, 2011, **111**, 3858-3887.
4. M. Hu, J. Chen, Z.-Y. Li, L. Au, G. V. Hartland, X. Li, M. Marquez and Y. Xia, *Chemical Society Reviews*, 2006, **35**, 1084-1094.
5. W. Lin, *Chemical Reviews*, 2015, **115**, 10407-10409.
6. M. Rycenga, C. M. Cobley, J. Zeng, W. Li, C. H. Moran, Q. Zhang, D. Qin and Y. Xia, *Chemical Reviews*, 2011, **111**, 3669-3712.
7. S. E. Skrabalak, J. Chen, Y. Sun, X. Lu, L. Au, C. M. Cobley and Y. Xia, *Accounts of Chemical Research*, 2008, **41**, 1587-1595.
8. K. Watanabe, D. Menzel, N. Nilius and H.-J. Freund, *Chemical Reviews*, 2006, **106**, 4301-4320.
9. K. D. Gilroy, A. Ruditskiy, H.-C. Peng, D. Qin and Y. Xia, *Chemical Reviews*, 2016, **116**, 10414-10472.
10. D. M. Alonso, S. G. Wettstein and J. A. Dumesic, *Chem Soc Rev*, 2012, **41**, 8075-8098.
11. S. E. Habas, H. Lee, V. Radmilovic, G. A. Somorjai and P. Yang, *Nat Mater*, 2007, **6**, 692-697.
12. C. J. DeSantis, R. G. Weiner, A. Radmilovic, M. M. Bower and S. E. Skrabalak, *The Journal of Physical Chemistry Letters*, 2013, **4**, 3072-3082.
13. X. Liu, D. Wang and Y. Li, *Nano Today*, 2012, **7**, 448.
14. D. Wang and Y. Li, *Advanced Materials*, 2011, **23**, 1044-1060.
15. M. Sankar, N. Dimitratos, P. J. Miedziak, P. P. Wells, C. J. Kiely and G. J. Hutchings, *Chem. Soc. Rev.*, 2012, **41**, 8099.
16. R. Ferrando, J. Jellinek and R. L. Johnston, *Chemical Reviews*, 2008, **108**, 845-910.
17. M. B. Cortie and A. M. McDonagh, *Chemical Reviews*, 2011, **111**, 3713-3735.
18. T. Chen and V. O. Rodionov, *ACS Catalysis*, 2016, **6**, 4025-4033.
19. B. Goris, G. Guzzinati, C. Fernández-López, J. Pérez-Juste, L. M. Liz-Marzán, A. Trügler, U. Hohenester, J. Verbeeck, S. Bals and G. Van Tendeloo, *The Journal of Physical Chemistry C*, 2014, **118**, 15356-15362.
20. W. H. Qi and S. T. Lee, *The Journal of Physical Chemistry C*, 2010, **114**, 9580-9587.
21. R. Liu, J. Guo, G. Ma, P. Jiang, D. Zhang, D. Li, L. Chen, Y. Guo and G. Ge, *ACS Applied Materials & Interfaces*, 2016, **8**, 16833-16844.
22. C. Li, L. Sun, Y. Sun and T. Teranishi, *Chemistry of Materials*, 2013, **25**, 2580-2590.
23. D. Seo, C. I. Yoo, J. Jung and H. Song, *Journal of the American Chemical Society*, 2008, **130**, 2940-2941.
24. B. Lim, M. Jiang, P. H. C. Camargo, E. C. Cho, J. Tao, X. Lu, Y. Zhu and Y. Xia, *Science*, 2009, **324**, 1302-1305.
25. W. Yu, M. D. Porosoff and J. G. Chen, *Chemical Reviews*, 2012, **112**, 5780-5817.
26. Y.-J. Wang, N. Zhao, B. Fang, H. Li, X. T. Bi and H. Wang, *Chemical Reviews*, 2015, **115**, 3433-3467.

27. C. L. Bracey, P. R. Ellis and G. J. Hutchings, *Chemical Society Reviews*, 2009, **38**, 2231-2243.
28. N. Wang, Y. Han, Y. Xu, C. Gao and X. Cao, *Analytical Chemistry*, 2015, **87**, 457-463.
29. C.-Y. Tai, J.-L. Chang, J.-F. Lee, T.-S. Chan and J.-M. Zen, *Electrochimica Acta*, 2011, **56**, 3115-3121.
30. M.-C. Daniel and D. Astruc, *Chemical Reviews*, 2004, **104**, 293-346.
31. M. Stratakis and H. Garcia, *Chemical Reviews*, 2012, **112**, 4469-4506.
32. K. Saha, S. S. Agasti, C. Kim, X. Li and V. M. Rotello, *Chemical Reviews*, 2012, **112**, 2739-2779.
33. W. Zhou, X. Gao, D. Liu and X. Chen, *Chemical Reviews*, 2015, **115**, 10575-10636.
34. G. J. Hutchings, *Catalysis Today*, 2002, **72**, 11-17.
35. A. S. K. Hashmi and G. J. Hutchings, *Angewandte Chemie International Edition*, 2006, **45**, 7896-7936.
36. G. J. Hutchings, *Journal of Materials Chemistry*, 2009, **19**, 1222-1235.
37. M. B. Gawande, A. Goswami, F.-X. Felpin, T. Asefa, X. Huang, R. Silva, X. Zou, R. Zboril and R. S. Varma, *Chemical Reviews*, 2016, **116**, 3722-3811.
38. D. Zhang, R. Wang, M. Wen, D. Weng, X. Cui, J. Sun, H. Li and Y. Lu, *Journal of the American Chemical Society*, 2012, **134**, 14283-14286.
39. A. A. Peterson, F. Abild-Pedersen, F. Studt, J. Rossmeisl and J. K. Norskov, *Energy & Environmental Science*, 2010, **3**, 1311-1315.
40. I. Pastoriza-Santos, A. Sánchez-Iglesias, B. Rodríguez-González and L. M. Liz-Marzán, *Small*, 2009, **5**, 440-443.
41. M. Jin, G. He, H. Zhang, J. Zeng, Z. Xie and Y. Xia, *Angewandte Chemie International Edition*, 2011, **50**, 10560-10564.
42. P. Lignier, R. Bellabarba and R. P. Tooze, *Chemical Society Reviews*, 2012, **41**, 1708-1720.
43. Y. Wang and T. Asefa, *Langmuir*, 2010, **26**, 7469-7474.
44. H. Guo, X. Liu, Q. Xie, L. Wang, D.-L. Peng, P. S. Branco and M. B. Gawande, *RSC Advances*, 2013, **3**, 19812-19815.
45. M. B. Gawande, A. Goswami, T. Asefa, H. Guo, A. V. Biradar, D.-L. Peng, R. Zboril and R. S. Varma, *Chemical Society Reviews*, 2015, **44**, 7540-7590.
46. K. P. Rice, E. J. Walker, M. P. Stoykovich and A. E. Saunders, *The Journal of Physical Chemistry C*, 2011, **115**, 1793-1799.
47. G. H. Chan, J. Zhao, E. M. Hicks, G. C. Schatz and R. P. Van Duyne, *Nano Letters*, 2007, **7**, 1947-1952.
48. L. Balogh and D. A. Tomalia, *Journal of the American Chemical Society*, 1998, **120**, 7355-7356.
49. P. Pulkkinen, J. Shan, K. Leppänen, A. Känsäkoski, A. Laiho, M. Järn and H. Tenhu, *ACS Applied Materials & Interfaces*, 2009, **1**, 519-525.
50. S. Pace, T. Van Hoof, M. Hou, C. Buess-Herman and F. Reniers, *Surface and Interface Analysis*, 2004, **36**, 1078-1082.
51. Z. Xu, E. Lai, Y. Shao-Horn and K. Hamad-Schifferli, *Chemical Communications*, 2012, **48**, 5626-5628.
52. X. Liu, A. Wang, X. Wang, C.-Y. Mou and T. Zhang, *Chemical Communications*, 2008, 3187-3189.

53. A. K. Sra and R. E. Schaak, *Journal of the American Chemical Society*, 2004, **126**, 6667-6672.
54. A. K. Sra, T. D. Ewers and R. E. Schaak, *Chemistry of Materials*, 2005, **17**, 758-766.
55. R. J. Chimentão, F. Medina, J. L. G. Fierro, J. Llorca, J. E. Sueiras, Y. Cesteros and P. Salagre, *Journal of Molecular Catalysis A: Chemical*, 2007, **274**, 159-168.
56. C. Della Pina, E. Falletta and M. Rossi, *Journal of Catalysis*, 2008, **260**, 384-386.
57. K. Miyajima, N. Fukushima, H. Himeno, A. Yamada and F. Mafuné, *The Journal of Physical Chemistry A*, 2009, **113**, 13448-13450.
58. K. Miyajima, H. Himeno, A. Yamada, H. Yamamoto and F. Mafuné, *The Journal of Physical Chemistry A*, 2011, **115**, 1516-1520.
59. H. Okamoto, D. J. Chakrabarti, D. E. Laughlin and T. B. Massalski, *Bull. Alloy Phase Diagrams*, 1987, **8**, 454–473.
60. G. Guisbiers, S. Mejia-Rosales, S. Khanal, F. Ruiz-Zepeda, R. L. Whetten and M. José-Yacaman, *Nano Letters*, 2014, **14**, 6718-6726.
61. M. Cui, H. Lu, H. Jiang, Z. Cao and X. Meng, *Scientific Reports*, 2017, **7**, 41990.
62. J. Yin, S. Shan, L. Yang, D. Mott, O. Malis, V. Petkov, F. Cai, M. Shan Ng, J. Luo, B. H. Chen, M. Engelhard and C.-J. Zhong, *Chemistry of Materials*, 2012, **24**, 4662-4674.
63. N. E. Motl, A. F. Smith, C. J. DeSantis and S. E. Skrabalak, *Chemical Society Reviews*, 2014, **43**, 3823-3834.
64. M. Nasilowski, B. Mahler, E. Lhuillier, S. Ithurria and B. Dubertret, *Chemical Reviews*, 2016, **116**, 10934-10982.
65. Y. Xia, Y. Xiong, B. Lim and S. E. Skrabalak, *Angewandte Chemie International Edition*, 2009, **48**, 60-103.
66. H. Zhang, M. Jin and Y. Xia, *Angewandte Chemie International Edition*, 2012, **51**, 7656-7673.
67. T. K. Sau and A. L. Rogach, *Advanced Materials*, 2010, **22**, 1781-1804.
68. J.-F. Li, Y.-J. Zhang, S.-Y. Ding, R. Panneerselvam and Z.-Q. Tian, *Chemical Reviews*, 2017, **117**, 5002-5069.
69. Y. Yan, J. S. Du, K. D. Gilroy, D. Yang, Y. Xia and H. Zhang, *Advanced Materials*, 2017, **29**, 1605997-n/a.
70. N. T. K. Thanh, N. Maclean and S. Mahiddine, *Chemical Reviews*, 2014, **114**, 7610-7630.
71. Y. Xia, K. D. Gilroy, H.-C. Peng and X. Xia, *Angewandte Chemie International Edition*, 2017, **56**, 60-95.
72. B. Lim and Y. Xia, *Angewandte Chemie International Edition*, 2011, **50**, 76-85.
73. N. E. Motl, E. Ewusi-Annan, I. T. Sines, L. Jensen and R. E. Schaak, *The Journal of Physical Chemistry C*, 2010, **114**, 19263-19269.
74. L. Shi, A. Wang, Y. Huang, X. Chen, J. J. Delgado and T. Zhang, *European Journal of Inorganic Chemistry*, 2012, **2012**, 2700-2706.
75. Y. Liu and A. R. H. Walker, *Angewandte Chemie International Edition*, 2010, **49**, 6781-6785.
76. W. Chen, R. Yu, L. Li, A. Wang, Q. Peng and Y. Li, *Angewandte Chemie International Edition*, 2010, **49**, 2917-2921.
77. A. Henkel, A. Jakab, G. Brunklaus and C. Sönnichsen, *The Journal of Physical Chemistry C*, 2009, **113**, 2200-2204.
78. S. E. Lohse and C. J. Murphy, *Chemistry of Materials*, 2013, **25**, 1250-1261.

79. S. Chen, S. V. Jenkins, J. Tao, Y. Zhu and J. Chen, *The Journal of Physical Chemistry C*, 2013, **117**, 8924-8932.
80. S. Thota, S. Chen, Y. Zhou, Y. Zhang, S. Zou and J. Zhao, *Nanoscale*, 2015, **7**, 14652-14658.
81. R. He, Y.-C. Wang, X. Wang, Z. Wang, G. Liu, W. Zhou, L. Wen, Q. Li, X. Wang, X. Chen, J. Zeng and J. G. Hou, *Nat Commun*, 2014, **5**.
82. C. Cobley and Y. Xia, *Materials Science and Engineering R*, 2010, **70**, 44-62.
83. K. Gilroy, P. Farzinpour, A. Sundar, R. Hughes and S. Neretina, *Chemistry of Materials*, 2014, **26**, 3340–3347.
84. S. Thota, S. Chen and J. Zhao, *Chemical Communications*, 2016, **52**, 5593-5596.
85. S. Thota, Y. Zhou, S. Chen, S. Zou and J. Zhao, *Nanoscale*, 2017, **9**, 6128-6135.
86. G. G. Li, E. Villarreal, Q. Zhang, T. Zheng, J.-J. Zhu and H. Wang, *ACS Applied Materials & Interfaces*, 2016, **8**, 23920-23931.
87. A. N. Simonov, P. E. Plyusnin, Y. V. Shubin, R. I. Kvon, S. V. Korenev and V. N. Parmon, *Electrochimica Acta*, 2012, **76**, 344-353.
88. S. Yury, P. Pavel and S. Marat, *Nanotechnology*, 2012, **23**, 405302.
89. D. I. Potemkin, E. Y. Filatov, A. V. Zadesenets, P. V. Snytnikov, Y. V. Shubin and V. A. Sobyanin, *Chemical Engineering Journal*, 2012, **207-208**, 683-689.
90. D. I. Potemkin, E. Y. Semitut, Y. V. Shubin, P. E. Plyusnin, P. V. Snytnikov, E. V. Makotchenko, D. Y. Osadchii, D. A. Svintsitskiy, S. A. Venyaminov, S. V. Korenev and V. A. Sobyanin, *Catalysis Today*, 2014, **235**, 103-111.
91. J. Luo, M. M. Maye, V. Petkov, N. N. Kariuki, L. Wang, P. Njoki, D. Mott, Y. Lin and C.-J. Zhong, *Chemistry of Materials*, 2005, **17**, 3086-3091.
92. B. N. Wanjala, J. Luo, B. Fang, D. Mott and C.-J. Zhong, *Journal of Materials Chemistry*, 2011, **21**, 4012-4020.
93. D. Kim, C. Xie, N. Becknell, Y. Yu, M. Karamad, K. Chan, E. J. Crumlin, J. K. Nørskov and P. Yang, *J. Am. Chem. Soc.*, 2017, **139**, 8329-8336.
94. G. Wang, L. Xiao, B. Huang, Z. Ren, X. Tang, L. Zhuang and J. Lu, *Journal of Materials Chemistry*, 2012, **22**, 15769-15774
95. H. Prunier, J. Nelayah, C. Ricolleau, G. Wang, S. Nowak, A.-F. Lamic-Humblot and D. Alloyeau, *Physical Chemistry Chemical Physics*, 2015, **17**, 28339-28346
96. D. Kim, J. Resasco, Y. Yu, A. M. Asiri and P. Yang, *Nat Commun*, 2014, **5**.
97. A. Sánchez-Iglesias, N. Winckelmans, T. Altantzis, S. Bals, M. Grzelczak and L. M. Liz-Marzán, *Journal of the American Chemical Society*, 2017, **139**, 107-110.
98. M. G. Blaber, M. D. Arnold and M. J. Ford, *Journal of Physics: Condensed Matter*, 2010, **22**, 143201.
99. E. M. Perassi, C. Hrelescu, A. Wisnet, M. Döblinger, C. Scheu, F. Jäckel, E. A. Coronado and J. Feldmann, *ACS Nano*, 2014, **8**, 4395-4402.
100. S. Linic, P. Christopher and D. B. Ingram, *Nat Mater*, 2011, **10**, 911-921.
101. Y. Ma, W. Li, E. C. Cho, Z. Li, T. Yu, J. Zeng, Z. Xie and Y. Xia, *ACS Nano*, 2010, **4**, 6725-6734.
102. Y. H. Lee, H. Chen, Q.-H. Xu and J. Wang, *The Journal of Physical Chemistry C*, 2011, **115**, 7997-8004.
103. S. Guo, S. Zhang, X. Sun and S. Sun, *Journal of the American Chemical Society*, 2011, **133**, 15354-15357.

104. Y. Ding, F. Fan, Z. Tian and Z. L. Wang, *Journal of the American Chemical Society*, 2010, **132**, 12480-12486.
105. A. I. Frenkel, V. S. Machavariani, A. Rubshtein, Y. Rosenberg, A. Voronel and E. A. Stern, *Physical Review B*, 2000, **62**, 9364-9371.
106. T. Shibata, B. A. Bunker, Z. Zhang, D. Meisel, C. F. Vardeman and J. D. Gezelter, *Journal of the American Chemical Society*, 2002, **124**, 11989-11996.
107. H.-R. M. Jhong, S. Ma and P. J. A. Kenis, *Current Opinion in Chemical Engineering*, 2013, **2**, 191-199.
108. K. P. Kuhl, E. R. Cave, D. N. Abram and T. F. Jaramillo, *Energy & Environmental Science*, 2012, **5**, 7050-7059.
109. C. W. Li and M. W. Kanan, *Journal of the American Chemical Society*, 2012, **134**, 7231-7234.
110. W. Tang, A. A. Peterson, A. S. Varela, Z. P. Jovanov, L. Bech, W. J. Durand, S. Dahl, J. K. Norskov and I. Chorkendorff, *Physical Chemistry Chemical Physics*, 2012, **14**, 76-81.
111. Y. Chen and M. W. Kanan, *Journal of the American Chemical Society*, 2012, **134**, 1986-1989.
112. Y. Chen, C. W. Li and M. W. Kanan, *Journal of the American Chemical Society*, 2012, **134**, 19969-19972.
113. M. Gattrell, N. Gupta and A. Co, *Journal of Electroanalytical Chemistry*, 2006, **594**, 1-19.
114. B. A. Rosen, A. Salehi-Khojin, M. R. Thorson, W. Zhu, D. T. Whipple, P. J. A. Kenis and R. I. Masel, *Science*, 2011.
115. Z. D. Pozun, S. E. Rodenbusch, E. Keller, K. Tran, W. Tang, K. J. Stevenson and G. Henkelman, *The Journal of Physical Chemistry C*, 2013, **117**, 7598-7604.
116. T. Vincent and E. Guibal, *Langmuir*, 2003, **19**, 8475-8483.
117. E. Fuguet, C. Ràfols, E. Bosch and M. Rosés, *Langmuir*, 2003, **19**, 55-62.
118. K. Kuroda, T. Ishida and M. Haruta, *Journal of Molecular Catalysis A: Chemical*, 2009, **298**, 7-11.
119. C. Li, P. Wang, Y. Tian, X. Xu, H. Hou, M. Wang, G. Qi and Y. Jin, *ACS Catalysis*, 2017, 5391-5398.
120. J. Lee, J. C. Park and H. Song, *Advanced Materials*, 2008, **20**, 1523-1528.
121. E. Menumerov, R. A. Hughes and S. Neretina, *Nano Letters*, 2016, **16**, 7791-7797.
122. E. Menumerov, K. D. Gilroy, M. Hajfathalian, C. J. Murphy, E. R. McKenzie, R. A. Hughes and S. Neretina, *Catalysis Science & Technology*, 2016, **6**, 5737-5745.
123. J. G. Chen, C. A. Menning and M. B. Zellner, *Surface Science Reports*, 2008, **63**, 201-254.
124. B. Hammer and J. K. Norskov, *Nature*, 1995, **376**, 238-240.
125. D. M. Newns, *Physical Review*, 1969, **178**, 1123-1135.
126. M. Hajfathalian, K. D. Gilroy, A. Yaghoubzade, A. Sundar, T. Tan, R. A. Hughes and S. Neretina, *The Journal of Physical Chemistry C*, 2015, **119**, 17308-17315.
127. J. C. Bauer, D. Mullins, M. Li, Z. Wu, E. A. Payzant, S. H. Overbury and S. Dai, *Physical Chemistry Chemical Physics*, 2011, **13**, 2571-2581.
128. X. Liu, A. Wang, L. Li, T. Zhang, C.-Y. Mou and J.-F. Lee, *Journal of Catalysis*, 2011, **278**, 288-296.

129. W. Zhan, J. Wang, H. Wang, J. Zhang, X. Liu, P. Zhang, M. Chi, Y. Guo, Y. Guo, G. Lu, S. Sun, S. Dai and H. Zhu, *Journal of the American Chemical Society*, 2017, **139**, 8846-8854.
130. J. Ding, X. Li, L. Chen, X. Zhang and X. Tian, *Applied Catalysis B: Environmental*, 2018, **224**, 322-329.
131. E. Bonmatı´, A. Casanovas, I. Angurell and J. Llorca, *Topics in Catalysis*, 2014, **58**, 77-84.
132. S. t. Neatų, J. A. Macia-Agullo, P. Concepcion and H. Garcia, *J. Am. Chem. Soc.*, 2014, **136**, 15969–15976.
133. S. K. Cushing, J. Li, F. Meng, T. R. Senty, S. Suri, M. Zhi, M. Li, A. D. Bristow and N. Wu, *J. Am. Chem. Soc.*, 2012, **134**, 15033–15041.
134. E. B. Dickerson, E. C. Dreaden, X. Huang, I. H. El-Sayed, H. Chu, S. Pushpanketh, J. F. McDonald and M. A. El-Sayed, *Cancer Letters*, 2008, **269**, 57-66.
135. C. Ayala-Orozco, C. Urban, M. W. Knight, A. S. Urban, O. Neumann, S. W. Bishnoi, S. Mukherjee, A. M. Goodman, H. Charron, T. Mitchell, M. Shea, R. Roy, S. Nanda, R. Schiff, N. J. Halas and A. Joshi, *ACS Nano*, 2014, **8**, 6372-6381.
136. R. Bardhan, W. Chen, M. Bartels, C. Perez-Torres, M. F. Botero, R. W. McAninch, A. Contreras, R. Schiff, R. G. Pautler, N. J. Halas and A. Joshi, *Nano Letters*, 2010, **10**, 4920-4928.
137. R. Bardhan, N. K. Grady, J. R. Cole, A. Joshi and N. J. Halas, *ACS Nano*, 2009, **3**, 744-752.
138. S. K. Cushing and N. Wu, *The Journal of Physical Chemsitry letters*, 2016, **7**, 666-675.
139. N. Wu, *Nanoscale*, 2018, **10**, 2679-2696.